

# Forward tracking at the next $e^+e^-$ collider part II: experimental challenges and detector design

S. Aplin<sup>a</sup> M. Boronat<sup>b</sup> D. Dannheim<sup>c</sup> J. Duarte<sup>d</sup> F. Gaede<sup>a</sup>  
A. Ruiz-Jimeno<sup>d</sup> A. Sailer<sup>c</sup> M. Valentan<sup>e</sup> I. Vila<sup>d</sup> M. Vos<sup>b,\*</sup>

<sup>a</sup>*Deutsche Elektronen Synchrotron, Hamburg, Germany*

<sup>b</sup>*IFIC (U. Valencia/CSIC), Apd. Correos 22085, E-46071 Valencia, Spain*

<sup>c</sup>*CERN, CH-1211 Geneva 23, Switzerland*

<sup>d</sup>*IFCA (U. Cantabria/CSIC), A. de los Castros s/n, E-39005 Santander, Spain*

<sup>e</sup>*HEPHY, Nikolsdorfer Gasse 18, 1050 Vienna, Austria*

---

## Abstract

We present the second in a series of studies into the forward tracking system for a future linear  $e^+e^-$  collider with a center-of-mass energy in the range from 250 GeV to 3 TeV. In this note a number of specific challenges are investigated, that have caused a degradation of the tracking and vertexing performance in the forward region in previous experiments. We perform a quantitative analysis of the dependence of the tracking performance on detector design parameters and identify several ways to mitigate the performance loss for charged particles emitted at shallow angle.

*Key words:* Forward tracking, future linear  $e^+e^-$  collider, ILC, CLIC

---

## 1 Introduction

A high-luminosity, high-energy, linear  $e^+e^-$  collider yields excellent opportunities for precision tests of the Standard Model of particle physics. The combination of precisely calculable electroweak production and strict control of the initial state with the relatively benign experimental environment and state-of-the-art detector systems allow for a characterization of Standard Model and

---

\* Corresponding author. E-mail: marcel.vos@ific.uv.es

new physics processes with a precision that goes well beyond what can be achieved at hadron colliders.

Two projects exist that pursue the creation of a linear electron-positron collider (referred to as Linear Colliders or LC in the remainder of this note):

- The proposal for an International Linear Collider (ILC [1]) is based on existing super-conducting Radio-Frequency (RF) cavity technology. In the baseline design the ILC is envisaged to reach a center-of-mass energy of 500 GeV. Early stages of the physics programme are likely to involve running at a center-of-mass energy of 250–350 GeV to study the properties and couplings of the Higgs boson and to characterize the production threshold for  $t\bar{t}$  pair production. The possibility to upgrade the ILC to a maximum of  $\sqrt{s} = 1$  TeV is a crucial requirement to the design.
- To reach larger center-of-mass energies, the accelerating gradient obtained in the previous scheme is insufficient. The Compact Linear Collider (CLIC [2]) aims to open up the energy regime up to several TeV using a novel technology, where a drive beam is used to provide power to the room temperature RF cavities of the main Linac.

The physics case for a linear  $e^+e^-$  machine has been made in great detail in References [3,4,5,6,7,8,9]. The specific case of a multi-TeV  $e^+e^-$  collider is discussed in References [10,11,12]. Recently, the focus has naturally shifted to a precise determination of the properties of the boson [13,14] discovered at the Large Hadron Collider (LHC). However, a linear collider that covers the energy regime from several hundreds of GeV to several TeV offers a much broader programme of Standard Model measurements and searches for new phenomena. The interplay of the broader LC programme with respect to the LHC is studied in Reference [3,15].

A very active programme exists aimed at the development of detectors for a linear collider [16]. Innovative approaches towards calorimetry, tracking and vertex detectors are pursued in detector R & D collaborations. Two detector concept groups have prepared complete detector designs [17,18]. The same two detector concepts have been adapted to the CLIC environment [10].

In a previous article [19] we discussed the relevance of the detector performance at small polar angle for a number of key LC physics analyses. It is found that increasingly abundant many-fermion final states are often not contained in the central detector. We have moreover identified several potentially important processes, such as di-boson production, t-channel production of new particles, or Higgs boson production through vector boson fusion, that exhibit a strong preference for the forward region. This study established that, as the center-of-mass energy enters the 0.5-3 TeV regime, the track reconstruction

performance in the polar angle<sup>1</sup> region from  $5^\circ < \theta < 30^\circ$ , corresponding to  $87 \text{ mrad} < \theta < 520 \text{ mrad}$ , or  $0.87 < \cos \theta < 0.996$ , acquires a much greater relevance than at previous  $e^+e^-$  colliders.

Reconstruction of charged particles in the polar angle range from  $5^\circ < \theta < 30^\circ$  faces a number of specific challenges. The forward tracker in many experiments has not performed as well as the central tracker in key aspects like the momentum resolution, vertex reconstruction performance or the material budget. The aim of this paper is to quantify these effects and explore ways to mitigate their impact on the overall physics output of the experiment.

This paper is organized as follows. Section 2 provides a brief introduction of the LC detector concepts. The software and tools used to perform the simulation studies are briefly outlined in Section 3. In the subsequent sections we provide quantitative results on the following aspects of the tracker performance:

- Section 4: the contribution of beam-induced backgrounds to the hit density.
- Section 5: the momentum measurement for charged particles.
- Section 6: the reconstruction of the primary and secondary production vertices of charged particles.
- Section 7: the pattern recognition capabilities of the detector.

In Section 8 we summarize the findings. In an appendix a number of technicalities of forward tracking are discussed.

## 2 Detector concepts

Most collider experiments adopt a cylindrically symmetric geometry where the magnetic field in the tracking volume is provided by a large solenoid. This is the case for all ILC and CLIC detector concepts proposed until today. Many of the challenges of the forward tracking region are closely related to this geometry and are relatively insensitive to the details of the detector design. In many cases we can expose the dependence of the performance on detector design parameter by studying a generic simplified geometry.

To provide more quantitative and realistic estimates of the tracking performance, however, one needs to fill in the details of the detector design. In this

---

<sup>1</sup> Our notation corresponds to the usual cylindrical coordinates, where the  $z$ -axis coincides with the beam line and the field lines of the solenoidal magnetic field,  $r$  denotes the radial distance from the beam line in the plane perpendicular to  $z$  and  $\phi$  is the azimuthal angle. We also use the polar angle  $\theta$  that varies from  $\theta = 0^\circ$  when the vector is aligned with the beam line, to  $\theta = 90^\circ$  when it is perpendicular.

note we consider a detailed detector concept developed for the ILC [17] and later adapted to the CLIC environment [10].

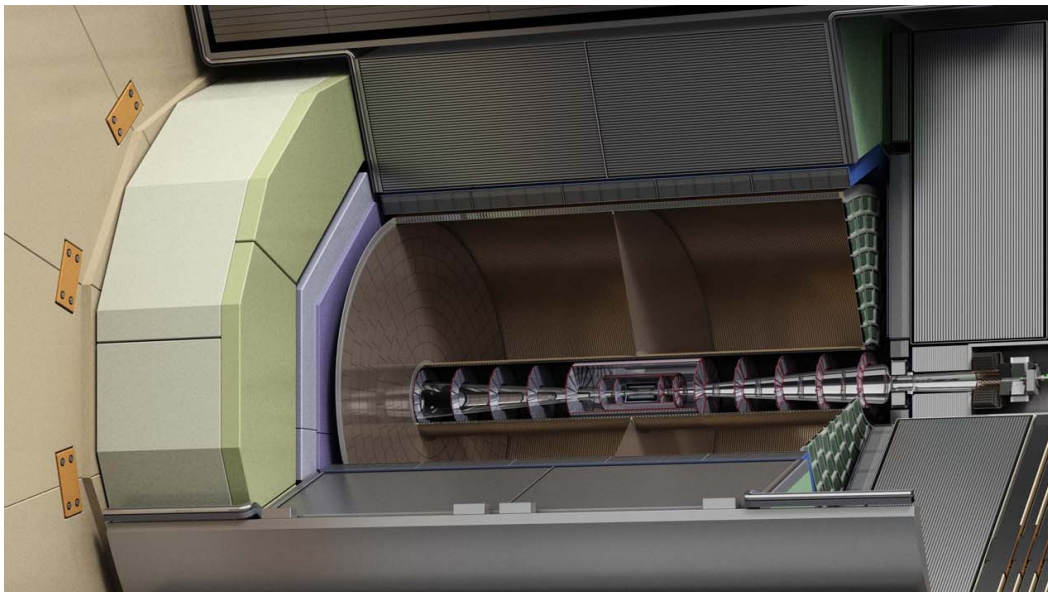


Fig. 1. A lateral view of the innermost part of the ILD detector. Figure prepared for the ILD Detailed Baseline Design [20].

A lateral view of a quadrant of the ILD detector is shown in Figure 1. A brief description of the most important features of the ILD and SiD [18] detector concept follows.

Both concepts are based on the particle flow concept that combines the energy measurements of different sub-systems – the tracker information for charged particles, the electromagnetic calorimeter for photons, and the hadronic calorimeter for neutral hadrons – to achieve an unprecedented jet energy resolution. The inner layers of the calorimeter system are formed by a highly granular Si-W calorimeter. In the outer layers iron may be used as absorber material (but running at a center-of-mass energy of one TeV and beyond may require tungsten also for the hadronic calorimeter to achieve a compact system that can contain hadronic showers of highly energetic particles). The granularity is also reduced to the level that relatively large cells (made of scintillating material) can yield an accurate measurement of the particle multiplicity. The calorimeter system is inserted in a superconducting solenoid that provides an approximately axial magnetic field with a strength of 3.5 Tesla for ILD (4 Tesla in the CLIC variant of the detector concept) and 5 Tesla for SiD.

Both concepts envisage a conical beam pipe that limits the acceptance of the tracking system to approximately  $5^\circ < \theta < 175^\circ$ . In the Silicon Detector concept the entire tracking volume is instrumented with silicon-based devices. A compact pixel detector close to the interaction point acts as a vertex detector. The 5 cylindrical layers in the *barrel* part of the detector are complemented by

*end-cap* disks to provide nearly uniform five-point coverage down to a polar angle of  $12.5^\circ$ . The vertex detector is surrounded by 5 barrel layers and 4 disks equipped silicon micro-strip detectors.

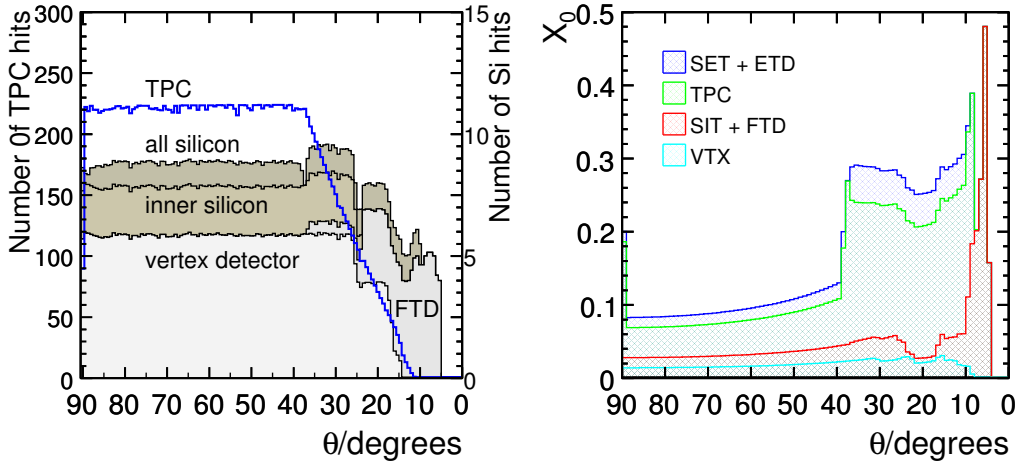


Fig. 2. Leftmost panel: the number of hits attached to 100 GeV muons in the gaseous and solid tracking subsystems versus polar angle  $\theta$  in the ILD design for the ILC. The number of hits in the TPC is referred to the leftmost axis. The number of hits in the silicon detectors (including the vertex detector) is indicated with different shadings of grey. Rightmost panel: the detector material in radiation lengths versus polar angle. The beam pipe is accounted for in the SIT+FTD material. Both figures are reproduced from Reference [17].

The ILD [17] detector relies on a large Time Projection Chamber for reconstruction of charged tracks. The vertex detector and innermost tracker layers are based on silicon pixel and micro-strip detectors, respectively. The choice of a smaller magnetic field (3.5 T instead of the 5 Tesla in SiD) drives the size of the detector. The outer envelope of the TPC is equipped with additional silicon micro-strip detectors. The polar angle coverage of the different subsystems of the ILD tracker is indicated in figure 2, where the number of hits attached to 100 GeV muons is shown as a function of polar angle. The Time Projection Chamber provides full coverage down to a polar angle of approximately  $37^\circ$ . Below that angle the number of read-out rings gradually decreases. The last TPC ring corresponds to a polar angle of just over  $10^\circ$ . The central innermost tracking system, consisting of the  $3 \times 2$  layers of the barrel vertex detector and the two layers of the Silicon Internal Tracker (SIT), provides eight precise measurements down to  $26^\circ$ . The innermost and middle double layer of the vertex detector extend out to approximately  $16^\circ$ . The seven Forward Tracking Disks (FTD) provide up to five measurements for tracks at small polar angle. The Silicon External Tracker (SET) and Endcap Tracking Disks (ETD) provide a precise space point with large lever arm down to approximately  $10^\circ$ .

The ILD tracking detectors are extremely transparent. A thin Beryllium beam pipe contributes 0.07% of a radiation length ( $X_0$ ). The material budget of

the vertex detector is 0.16%  $X_0$  per double ladder, each innermost Forward Tracking Disks contributes only 0.12%  $X_0$ , and the layers equipped with  $\mu$ -strip detectors represent 0.65%  $X_0$ /layer. Figure 2 clearly indicates how the material in the TPC is concentrated in the end-plate.

The design for the CLIC tracker elements is modified in several ways to cope with the increased in background levels [21]. The most important modification from the point of view of the overall detector performance is the increase in the radius of the innermost vertex detector layer ( $r = 2.6$  or  $3.1$  cm instead of the approximately  $1.5$  cm in both concepts for the ILC). Of particular importance for the forward tracking region is the end-cap system of the pixel vertex detector, that is added to the CLIC-ILD design to recover the forward coverage lost due to the increase of the inner radius of the barrel system. The redesign of the beam pipe leads to a slight loss of acceptance for very shallow tracks.

We have chosen to show results for the ILD concept. However, at the qualitative level all conclusions apply also to the SiD tracker.

### 3 Track reconstruction

An extensive set of tools is available to study the challenges of forward tracking at a quantitative level. We used two fast simulation packages, the Linear Collider detector toy, or LiCToy [22], and a custom setup based on the CMS track fitter. LiCToy uses an idealised helix model, with multiple Coulomb scattering, to simulate the particle trajectory in a solenoidal field, while the second package propagates the trajectories of charged particles through an arbitrary magnetic field map. A simplified detector geometry is constructed based on simple geometric shapes (cylinders and disks). The hit positions are smeared with a Gaussian or uniform distribution. In both packages the track fit is performed using a Kalman filter that takes into account interactions with the detector material.

The LC detector concepts have developed (*full*) simulation suites, relying on GEANT4 [23] to simulate the interactions of particles with a detailed detector model. We use the chain consisting of Mokka [24] for the interactions with the detector, the Marlin [25] package for reconstruction, and LCIO [26] to persistify objects. The LDCTracking package involves a track fit taking into account material effects. Recently, a completely new tracking software toolkit [27] was adopted by ILD, including a pattern recognition algorithm for the forward direction based on cellular automata [28].

The fast simulation tools were validated by comparing their results on a num-

ber of simple geometries. A further cross check was performed against the LCDTRK [29] package, that is based on an analytical calculation of the covariance matrices [30]. All codes are found to agree within errors when run on the same benchmark geometry.

### 3.1 Forward track reconstruction

In this paper we discuss a number of challenges of tracking in the forward region that are either not present or less severe in the central detector. Often, the forward region is considered even more special, so much so that it would require dedicated track reconstruction algorithms. In the following we argue, by means of an example, that general-purpose 3D trajectory propagation algorithms are adequate for the entire detector.

The trajectory of a charged particle in a uniform magnetic field is described by a helix. Five parameters are sufficient to describe the whole trajectory. For analytical calculations it is useful to break the helical trajectory down into two projections. In the  $r - \phi$  view our ideal particle describes a circle. In the  $r - z$  view the helical trajectory yields a sine wave, often approximated by a straight line for high momentum tracks. In Figure 3 we show these two projections for a particle leaves the interaction point (0,0,0) at a polar angle of  $45^\circ$ . In the uppermost Figure the track leaves hits on horizontal (barrel) layers with a small error in  $r\phi$  and a weak constraint on  $z$ . The second set of figures in the lowermost panel corresponds to the same particle traversing the *end-cap*.

In the past, limitations of CPU time and other resources have led experiments to use the analytical solution for an ideal particle in the  $r\phi$  and  $rz$  projections for track finding or even the final track fit. In the projections barrel and end-cap provide a different set of constraints on the trajectory. In the  $r\phi$  projection the trajectory, and in particular the momentum, is less constrained by the *end-cap* detector.

In the last decades, however, a sophisticated machinery has been developed to deal with the fully general case. Numerical 3D trajectory propagation allows to remove the evident limitations of the analytical approach, by taking into account energy loss and multiple scattering in detector material and by performing the propagation with a realistic magnetic field. All modern experiments use this much more general approach in the final track fit. Even in areas, such as pattern recognition or the trigger, where one used to resort to a simpler treatment, the 3D formalism is rapidly taking over. It seems safe, therefore, to assume the ILC or CLIC experiments will have access to the general 3D treatment at all stages of track reconstruction, including track finding.

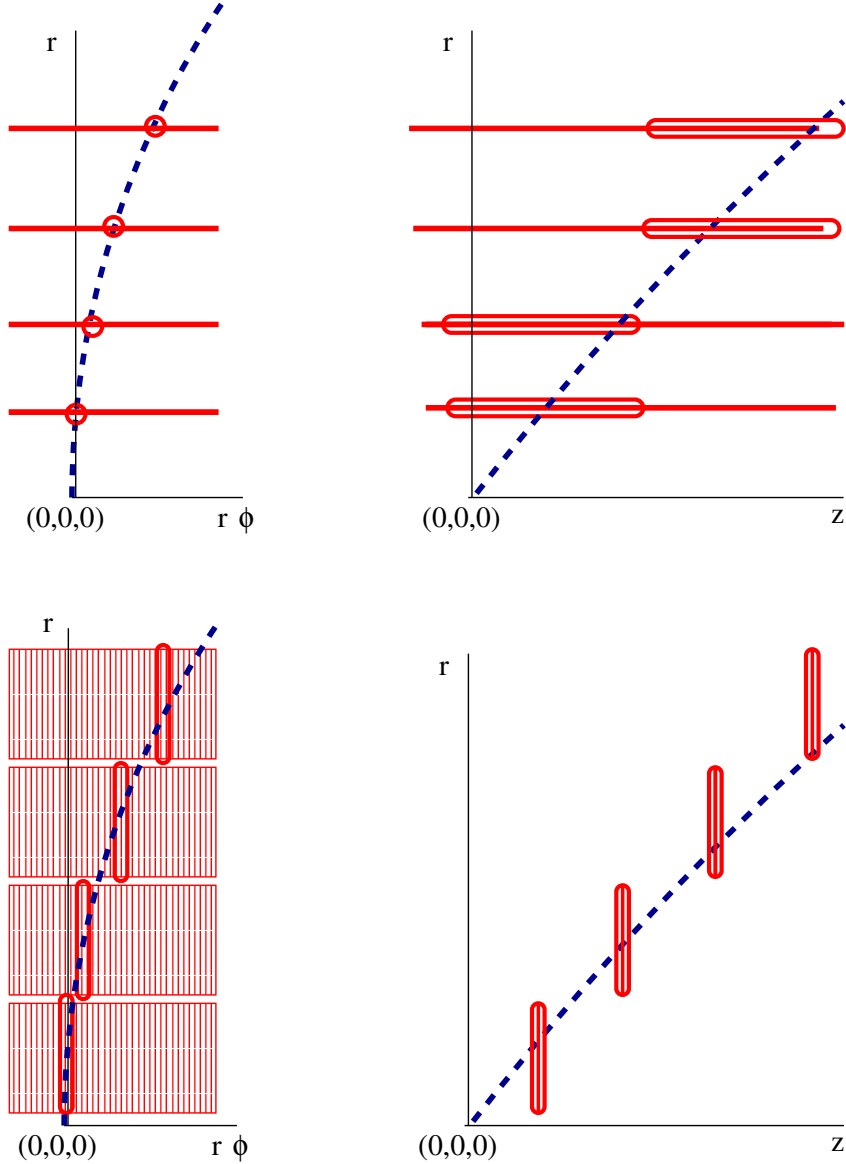


Fig. 3. The projections of a helix trajectory on the  $r\phi$  and  $rz$  planes. The hits on solid state detectors along the trajectory are indicated for two situations: the uppermost drawings represent a cylindrical *barrel* detector geometry and the lowermost drawings correspond to the *endcap* of the tracker.

Using the full 3-D information the trajectory of the particle at  $\theta = 45^\circ$  in our example is equally constrained by the barrel and end-cap setups. We find, using the CMS Kalman filter track fitter on a toy geometry, that this is indeed the case. The track parameter uncertainties in Figure 4 at  $\theta = 45^\circ$  are identical whether the track fit is fed with  $r\phi$  and  $z$  measurements on horizontal (*barrel*) layers or  $r\phi$  and  $r$  measurements on vertical disks.

The analytical approach with projections on the  $r\phi$  and  $rz$  planes has ceased to be relevant for the design of the experiment. There is no longer a need for



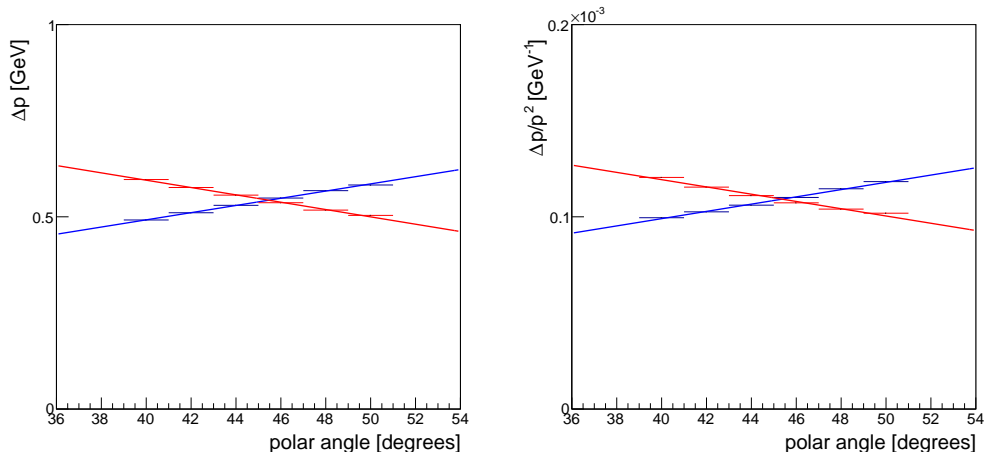


Fig. 4. The uncertainty on the transverse momentum (leftmost figure) and longitudinal momentum (rightmost figure) as a function of polar angle  $\theta$ . The results correspond to 100 GeV tracks emitted at a polar angle of close to  $45^\circ$  and measured in a toy detector, consisting of equally spaced cylindrical layers (blue lines) or disks (red lines). For  $\theta = 45^\circ$  both setups yield identical results.

dedicated algorithms to propagate or fit tracks in the forward detector.

#### 4 Environment: background

When two bunches of the ILC collide, beam particles radiate photons under the influence of the electromagnetic field of the opposite beam. These beamstrahlung photons convert into electron-positron pairs through several processes known as coherent and incoherent pair production. The interaction of the colliding bunches is modeled using a dedicated generator GuineaPig [31,32,33].

The electrons and positrons produced in the interaction between the colliding bunches are generally emitted at small angle with respect to the beam axis and with small momenta. In the intense magnetic field in the tracking volume, the large majority of background particles curl up in spirals with a small radius. If the downstream structures are carefully designed coherent pair production has a negligible contribution to the hit density of the detector. Incoherent pair production, on the other hand, produces a small but significant fraction of the electrons and positrons with a transverse momentum exceeding 100 MeV. The number of produced pairs and their  $p_T$  spectrum vary strongly with the final focus parameter and the center-of-mass energy, leading to an uncertainty of a factor 3–5 in the number of particles reaching the innermost elements of the tracker and vertex detector.

The  $\gamma\gamma \rightarrow$  hadrons process produces charged particles at a much lower rate

than the pair production processes. Due to the much harder momentum spectrum, however, charged particles can reach the outer layers of the detector, where this process is the dominant background source.

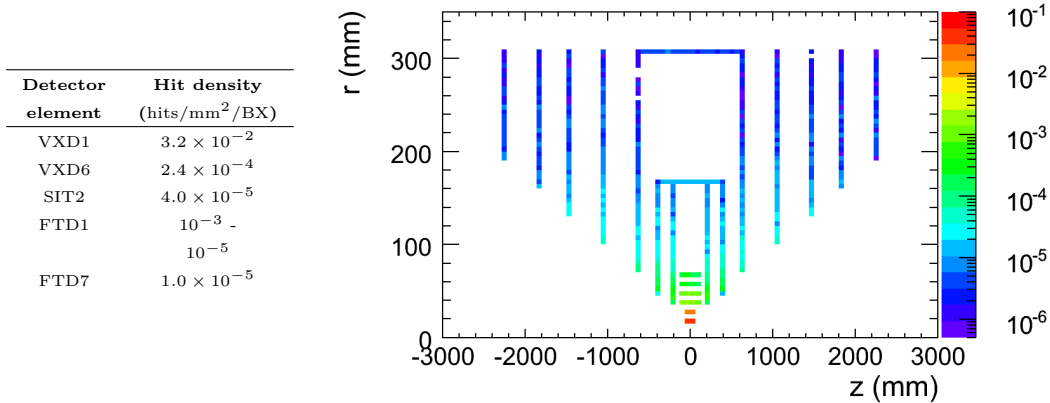


Fig. 5. Background levels due to incoherent pair production in the inner tracking system of the ILD detector concept for 500 GeV operation of the ILC (in hits/mm<sup>2</sup>/BX). The table shows average densities over the detector surface, except for the innermost vertex detector disk (VXEC1) and the innermost forward tracking disk (FTD1), where the densities at the innermost and outermost radius are shown separately. The figure is reproduced from Reference [17] and is based on the nominal set of final focus parameters.

The direct hits due to electrons or positrons with relatively large transverse momenta are complemented by hits due to particles reflected off the material that surrounds the beam pipe further up- or downstream (small angle calorimeter systems). The result of a complete GEANT4 [23] simulation of 100 bunch crossings in the ILD detector at the ILC is shown in Figure 5.

The forward region of the tracking system receives a non-negligible amount of background hits. The background hit density in the inner rings of the first three disks is of the order of several times  $10^{-4}$ hits/mm<sup>2</sup>/BX, comparable to that of the outermost vertex detector layers. Typically half of the hits on the forward tracking disks are due to particles reflected from upstream structures.

The occupancy due to background depends on the detector integration time with respect to the bunch structure of the collider. The envisaged bunch structures of ILC and CLIC are very different. For the ILC “cold technology” based on superconducting cavities it is foreseen that every 200 ms there is a very brief ( $\sim 1$  ms) bunch train consisting of 1312 bunches colliding at regular intervals of 500 ns. Existing detector concepts with a time resolution smaller than  $\sim 500$  ns can therefore distinguish individual bunch crossings at the ILC.

The hit density in the CLIC-ILD tracker layers due to incoherent pair production and  $\gamma\gamma \rightarrow$  hadrons, based on the study of Reference [34], is shown in Figure 6. The layout of the innermost layers is modified with respect to the

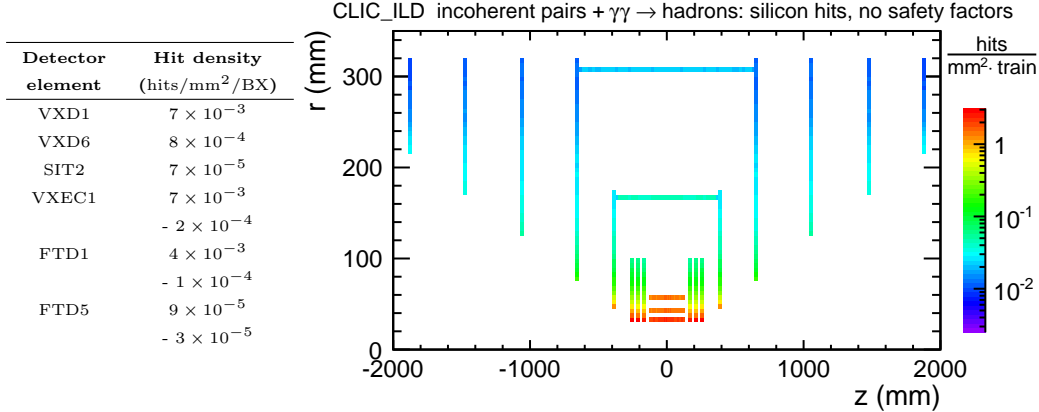


Fig. 6. The background hit density (in hits/mm<sup>2</sup>/bunch train) in the innermost tracking system of the ILD detector in the CLIC environment at  $\sqrt{s} = 3$  TeV. The contributions of incoherent pair production and  $\gamma\gamma \rightarrow$  hadrons are added. The table shows average densities over the detector surface, except for VXEC1, FTD1 and FTD5, where the densities at the innermost and outermost radius are shown separately.

background map for ILC in Figure 5. In particular, the innermost layer was moved to  $r = 3.1$  cm, instead of the 1.5 cm at the ILC [21]. The CLIC bunch structure is different as well; every 20 ns a short train of 312 bunches at 0.5 ns intervals collides. Sub-bunch train time-stamping at CLIC requires new read-out concepts to be developed. The results are therefore presented as the hit density per train of 312 bunch crossings. And, finally, the contribution of  $\gamma\gamma \rightarrow$  hadrons is included for CLIC. The contribution of incoherent pair production is dominant in all layers of the inner tracking system except for the barrel tracker (SIT) and for outer radii of the forward tracking disks, where the contribution of  $\gamma\gamma \rightarrow$  hadrons reaches a similar level [34].

The hit density in the forward tracker presents a constraint and a challenge to the design. To cope with the background levels a combination of fast read-out and high detector granularity is required.

## 5 Momentum resolution

The recoil-mass method to determine the couplings of the Higgs boson is a central piece of the LC physics programme. It requires excellent momentum reconstruction for muons with  $E \sim (\sqrt{s} - m_H)/2$  [35]. In a high-energy collider, a similar requirement is derived from the analysis of the  $H \rightarrow \mu^+\mu^-$  decay [36,37]. Therefore, all LC detector concepts aim for excellent momen-

tum resolution for charged tracks, usually specified as:

$$\Delta\left(\frac{1}{p}\right)[\text{GeV}]^{-1} = 2 \times 10^{-5} \oplus \frac{10^{-3}}{p[\text{GeV}]} \quad (1)$$

The first term applies to the asymptotic resolution for high momentum tracks, where multiple Coulomb scattering in the detector material is negligible. The second term constrains the material budget of the tracker. At this level the tracker resolution has negligible impact on the energy resolution of the particle flow algorithm:  $\Delta p_T/p_T \ll \Delta E_j/E_j$  for all relevant momenta.

Compared to previous experiments, the momentum resolution requirement of the linear collider experiments implies a very significant improvement. The LEP experiments reached  $5 \times 10^{-4} \text{ GeV}^{-1}$  [38,39]. The LHC general-purpose experiments quote a relative transverse momentum resolution  $\sigma(p_T)/p_T$  for central 100 GeV particles in the range from 1.5 % (CMS [40]) to 4 % (ATLAS [41]), corresponding to  $\Delta(1/p_T) = 1 - 4 \times 10^{-4} \text{ GeV}^{-1}$ .

In the following we discuss the dependence of the transverse momentum resolution on the polar angle. An important caveat must be kept in mind. The ability of the experiment to reconstruct narrow resonances decaying to pairs of charged particles depends on the precision of the total momentum measurement (rather than on that on the transverse momentum). Indeed, the total momentum is the relevant quantity for most physics analyses. It is therefore more reasonable to aim for a uniform resolution for the  $(1/p)$  measurement, than to require a constant  $\Delta(1/p_T)$  over the whole detector. As the polar angle at the production vertex is measured with excellent resolution the uncertainty on the total momentum is generally dominated by that on the transverse momentum:  $\Delta p_T/p_T \sim \Delta p/p$ . While in the central detector  $\Delta(1/p) = \Delta p/p^2$  and  $\Delta(1/p_T) = \Delta p_T/p_T^2$  are identical, in the forward region both quantities differ by a factor  $(\sin\theta)^{-1}$  (in the limit of perfect  $\theta$  measurement). This factor can be quite important, i.e. for tracks emitted at  $20^\circ$  the two quantities differ by nearly a factor three.

### 5.1 Performance & detector design

To expose the dependence on the parameters of the tracker design we consider an analytical approximation before turning to the simulation. The asymptotic momentum resolution for high-energy charged particles of a tracker consisting of  $N$  equally spaced layers<sup>2</sup> with spatial resolution  $\sigma_{r\phi}$  in a magnetic field  $B$

<sup>2</sup> The Gluckstern formula is valid for  $N > 10$ . But, even for only five space points involved in the track fit of the most forward particles, the exact numerical constant approaches  $\frac{720}{N+4}$  to within 7 %.

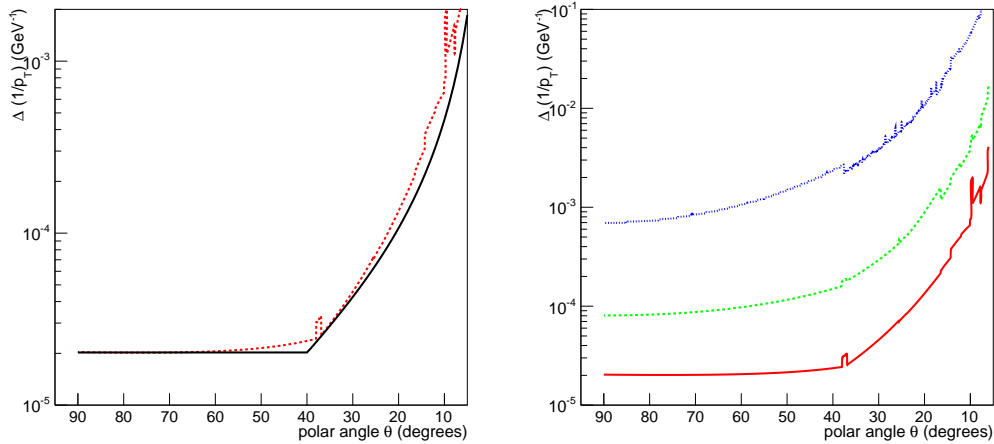


Fig. 7. The transverse momentum resolution versus polar angle  $\theta$  for single muons in the ILD detector, obtained with the LiC detector toy fast simulation [22,42]. In the leftmost panel the result for 100 GeV muons (dashed line) is compared to the prediction of the Gluckstern formula (continuous line). The spatial resolution of the latter is chosen such that the performance of the central detector is in good agreement. The three graphs in the rightmost panel correspond to momenta of 1 (blue dotted line), 10 (green dashed line) and 100 GeV (red continuous line).

(in Tesla) and with lever arm  $L$  perpendicular to the magnetic field (in meters) is given by [43]:

$$\frac{\sigma(p_T)}{p_T} = \sqrt{\frac{720}{N+4}} \sigma_{r\phi} \frac{p_T}{0.3BL^2}, \quad (2)$$

Assuming uniform quality of the instrumentation (i.e. all cylindrical layers and disk provide measurement with the same resolution  $\sigma_{r\phi}$  and adopting the aspect ratio of the ILD experiment, the asymptotic transverse momentum resolution in the absence of multiple scattering for 100 GeV tracks has the polar angle dependence shown in the leftmost panel of Figure 7. We find a considerable degradation of the performance, over more than an order magnitude, towards smaller polar angle. This is entirely due to the reduction of the projected length (on the transverse plane) of the trajectory  $L$ .

Superposed in the same Figure is the LiCToy result for the approximate ILD geometry. The curves follow each other rather closely for polar angles within the TPC acceptance (down to approximately  $25^\circ$ ). This is indication that the design provides rather uniform quality. In ILD this is achieved due to the partial cancellation of two effects; the decreasing number of space points in the TPC leads to a degradation at small polar angle that is more pronounced than the Gluckstern prediction in formula 2. The spatial resolution of the TPC depends, however, on the drift distance through the gas volume. The

parameterization in the simulation has [17]:

$$\sigma(r\phi)[\mu\text{m}] = 50\mu\text{m} \oplus 900\mu\text{m} \sin \phi \oplus 28\mu\text{m} \sin \theta \times \sqrt{\Delta z}[\text{cm}] \quad (3)$$

where  $\Delta z$  is the drift distance in centimeters. The resolution of space points close to the endplate is much improved. Therefore the forward performance recovers partially.

The momentum determination of the most shallow particles rests primarily on the measurements in the Forward Tracking Disks. For polar angles below  $16^\circ$  the number of measurements is reduced to 4-6. The simulation envisages a spatial resolution of  $7 \mu\text{m}$ , which is clearly insufficient to stay on the Gluckstern curve.

The discussion so far has focused on relatively high momentum tracks. The performance of a realistic tracker design for particles with a momentum below several tens of GeV is dominated by multiple scattering and thus depends crucially on a tight control of the detector material. LiCToy results for the transverse momentum resolution of particles with momenta of 100 GeV, 10 GeV and 1 GeV in the ILD detector are compared in Figure 7. In agreement with the functional form of equation 1 the resolution for 10 GeV particles is degraded by a factor 4 and that for 1 GeV particles by a factor 40. In the ultra-transparent tracker design of ILD the material term in equation 1 becomes comparable to the first term for  $p \sim 50$  GeV, the energy of muons from  $Z$ -decay in  $ZH$  production at  $\sqrt{s} = 250$  GeV.

## 5.2 Discussion

The parameters that govern the momentum resolution for forward tracks are highly constrained by the overall detector layout (and cost). A factor two improvement of the momentum resolution requires to double the magnetic field or the length along  $z$  of the tracking volume. Neither of these are viable in the ILD and SiD design, where the total cost of the experiment receives large contributions from the coil (whose cost is approximately proportional to the total stored energy) and the calorimeter system (whose cost scales roughly with the length). Additional measurement layers do provide a means to improve the momentum resolution for very high momentum tracks, but the extra material severely damages the ability of the experiment to precisely reconstruct the abundant low momentum tracks in the forward region. The parameter that remains is the precision of the space points. To achieve the best possible momentum resolution, detector R&D must pursue devices that provide better  $r\phi$  resolution without increasing the material budget.

## 6 Vertex reconstruction

The identification of heavy flavour jets through the displaced vertex of long-lived beauty and charm hadrons has proven to be a crucial technique in previous experiments. Even for 500 GeV to 1 TeV operation charged particles carrying the lifetime information in the jets are often quite soft. Therefore, flavour tagging depends crucially on the precise reconstruction of low momentum ( $< 10$  GeV) tracks, where multiple scattering dominates the performance.

### 6.1 Performance & detector design

The ILC detector concepts have drawn up severe requirements on the vertexing performance of their tracking systems. The goal is usually expressed in terms of the following parameterization of the transverse impact parameter resolution in a cylindrical vertex detector with uniform spatial resolution and material:

$$\Delta d_0[\mu\text{m}] = a[\mu\text{m}] \oplus \frac{b[\mu\text{m}]}{p[\text{GeV}] \sin^{3/2} \theta} \quad (4)$$

The LC concepts have formulated a goal of  $a = 5$ ,  $b = 10$ . The value of the material term  $b$  is increased to 15 in the CLIC requirement. To achieve excellent flavour tagging a similar resolution on the longitudinal impact parameter is required, as well as excellent two-track resolution.

The transverse impact parameter resolution requirement in equation 4 represents a considerable improvement over vertex detectors built at collider experiments to date; the constant term is better by a factor 2–4 than what was achieved at previous  $e^+e^-$  colliders and at the LHC. Achieving the requirement for the second (material) term is even more challenging; it has to decrease by a factor 6–10 with respect to most previous experiments. Indeed, the requirement in Formula 4 (together with the assumed inner radius of 15 mm) implies that the vertex detector must be built with a strict material budget of order 0.1% of a radiation length per layer, a factor three better than the best material term achieved so far (by the SLD vertex detector) with:

$$\Delta d_0[\mu\text{m}] = 9[\mu\text{m}] \oplus \frac{33[\mu\text{m}]}{p[\text{GeV}] \sin^{3/2} \theta}. \quad (5)$$

The  $\sin^{-3/2} \theta$  form for the polar angle dependence of the the impact parameter resolution (the second term in equation 4) can be understood as follows. The distance of the innermost barrel layer to the interaction point increases as  $\sin \theta$ . Multiple scattering is proportional to the square root of the material

thickness in radiation lengths [44]. For an ideal detector of constant thickness this is proportional to the path length through the detector, that grows as  $\sin \theta$ . Following the same argument we can rewrite equation 4 for the case of polar angles where the first measurement is on an end-cap disk:

$$\Delta d_0[\mu\text{m}] = a[\mu\text{m}] \oplus \frac{b[\mu\text{m}] \times \frac{L}{R}}{p[\text{GeV}] \cos^{3/2} \theta}. \quad (6)$$

Due to the different orientation of the disks the  $\sin^{-3/2} \theta$  dependence is replaced by a  $\cos^{-3/2} \theta$  form. The numerical constant  $b$  of equation 4 is multiplied by the ratio  $\frac{L}{R}$  of the distance  $L$  (along  $z$ ) of the disk to the interaction point and the inner radius  $R_i$  of the barrel detector. Note that equation 6 ignores the contribution of the beam pipe.

## 6.2 Simulation

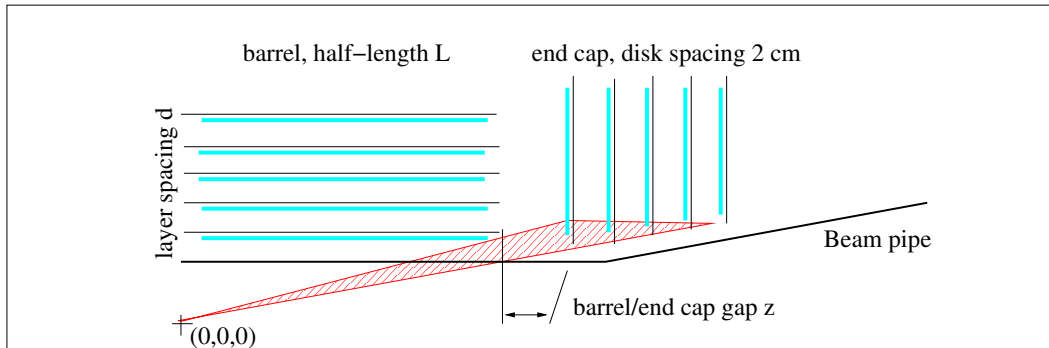


Fig. 8. The generic vertex detector layout. The choice of parameter is described in the text.

We evaluate the performance of the simplified layout shown schematically in figure 8. The most important parameter of the detector design is the inner radius of the innermost barrel layer and the disks. In particular the material term  $b$  is proportional to the inner radius [21]. In the ILC experiments the minimal distance is limited to approximately  $R \geq 15$  mm by the pair background. The CLIC vertex design envisages an inner radius of approximately 3.1 cm. To avoid the envelope of the intense core of pair production the beam pipe of the LC concepts has a conical shape beyond a certain  $|z|$ -value, such that in practice the minimum inner radius depends on the  $z$ -extension of the barrel or  $z$ -position of the disks.

The spatial resolution of the  $r\phi$  and  $z$  ( $r$ ) measurements of each layer (disk) is set to  $3 \mu\text{m}$ , the material to 0.12 % of a radiation length per layer. The gap between barrel and end cap structures must be minimized for optimal performance, within the boundary conditions due to mechanics and services. We consider  $z = 1$  cm. Finally, the spacing between layers has relatively little



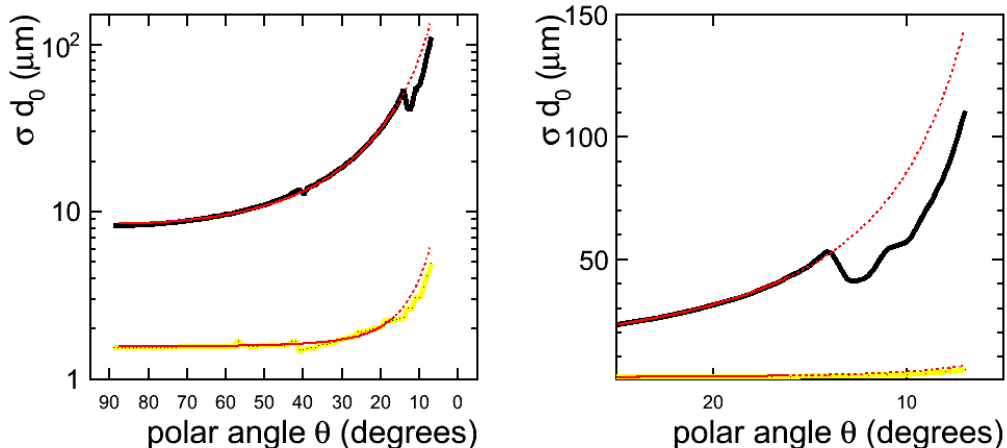


Fig. 9. The transverse impact parameter resolution versus polar angle  $\theta$  for single tracks in the toy vertex detector specified in the text. The two curves in the leftmost panel correspond to particles with a momentum of 1 GeV (black) and 100 GeV (yellow or grey). The functional form of equation 4 is fit to the result in the interval  $90^\circ < \theta < 17^\circ$  (red or dashed curves). The rightmost panel zooms in on the forward region.

impact on the performance and is fixed to  $d = 0.8$  cm and  $d = 2$  cm, in barrel and endcap, respectively.

The transverse impact parameter resolution of the ILC toy detector with  $R_i = 1.5$  cm is presented in Figure 9. The two curves correspond to particles with a momentum of 1 GeV (black) and 100 GeV (yellow/grey) and thus give an estimate of the  $b$  and  $a$  parameters, respectively. The functional form of equation 4 is fit to the result in the interval  $90 < \theta < 17^\circ$  (red/dashed curves). The parameterization yields an adequate description of the observed curve in the central region of the detector (this holds also for full simulation results). With these aggressive design assumptions the LC requirements are met in the central region. The parameter  $a$  in the constant term is less than 2, well below the required value of 5. A  $b$  parameter in the material term of 8 is achieved, again better than the required value of 10.

The functional form of equation 4 implies a steady degradation of the vertexing performance towards the forward region, that is inherent in the cylindrical layout of the barrel vertex detector. The degradation is certainly significant for 100 GeV particles, but the  $a$  term remains below 5 for the complete polar angle range considered. The material term  $b$  increases much more strongly. The combination of the larger extrapolation distance with the increase in the amount of material traversed by particles at shallow angle, has a strong impact on the performance. The uncertainty on  $d_0$  for low momentum particles doubles from 8 to 16  $\mu\text{m}$  before reaching  $30^\circ$  and doubles again between  $30^\circ$  and  $20^\circ$ .

The parameterization of equation 6 for particles that leave a first hit on an end-cap disk is found to be in qualitative agreement with the simulation. The zoom image of the forward region in the rightmost panel of Figure 9 indeed shows how the resolution improves sharply beyond the barrel-endcap transition at approximately  $15^\circ$ . This is primarily due to the reduced path length through the detector material. As the polar angle is reduced further the resolution improves until the coverage of the first disk is insufficient and a disk at greater z-distance from the interaction point takes over.

### 6.3 Discussion

One can see from the results of this simple model that a detector with a short barrel cuts off the  $\sin^{-3/2} \theta$  growth of the impact parameter resolution early and provides better performance at any polar angle. The rationale for the *long barrel* geometry adopted by ILD only becomes clear when more realism is added to the material budget. Even a minor contribution to the material budget in the conical region marked with a (red) fill pattern in Figure 8 leads to a severe degradation of the impact parameter of (low momentum) tracks emitted in that direction. It is noted here, however, that the long barrel layout cannot provide full polar angle coverage. The forward disks in this design are too distant from the interaction point to provide good performance. The vertexing performance for very shallow tracks is thus sacrificed.

The desire to keep the material in the “no-go” cone to an absolute minimum leads to a number of engineering challenges. Clearly, the beam pipe, that is traversed at an unfavourable angle, must be kept as thin as possible. A potentially even bigger threat are the services and support structures of the barrel vertex detector. To maintain good vertexing performance for particles that leave their first hit on the end-cap it is vital to route the services of the barrel over the end-cap. Also the supports and end-of-ladder area of the barrel vertex detector must avoid the “no-go” cone as much as possible.

## 7 Pattern recognition

The particle flow paradigm requires unambiguous association of all charged particle trajectories to energy deposits in the calorimeter. Confusion due to reconstruction inefficiency, badly reconstructed tracks or accidental combinations of hits yielding *fake* particle candidates must be kept to a minimum. The tracker at a linear collider experiment must therefore be capable of excellent pattern recognition.

A number of reasons render pattern recognition in the forward region of the detector more challenging than in the central detector:

- As discussed in Section 4 the hit density due to beam-induced background drops rapidly with increasing radial distance from the interaction point. The forward tracking devices closest to the beam pipe must therefore cope with severe background levels. This is further amplified by other background sources with a markedly forward profile like  $\gamma\gamma \rightarrow$  hadrons production.
- The strong magnetic field leads to an abundance of low momentum particles that leave the tracking volume curling through the forward tracking region (so called *loopers*). These represent a challenge to pattern recognition.
- The LC detector design have elongated tracking volumes, with an aspect ratio of approximately 75%. The larger distance between layers leads to a larger uncertainty on the extrapolated position on the next layer.

In this section we relate pattern recognition requirements to the detector design. We do not attempt to derive an analytic expression, as we did for the momentum resolution. Pattern recognition is, however, important in the formulation of the detector specifications. We present quantitative arguments in Section 7.1, based on the hit density of signal and background events, that motivate the choice for high-granularity devices in the innermost layers. We discuss the formation of ghost hits in  $\mu$ -strip detectors in Section 7.2 and put forward a detector design that minimizes their impact. We also discuss, in Section 7.3, the precision that should be required of the  $r$ -measurement of the tracking layers.

### 7.1 Detector occupancy

The foremost marker to optimize the detector granularity is the detector occupancy. At the LC it is safe to assume a single signal or physics event contributes to the detector occupancy. To this signal occupancy we must add the contribution of a certain number of beam-induced background events. The exact number of overlaid bunch crossings depends on the integration time and time stamping capabilities of the detector and may vary from one sub-system to the next. The total occupancy may be given as the sum of the occupancy from the physics event  $O_P$  and the background occupancy  $O_B$ . We determine a representative  $O_P$  in  $e^+e^- \rightarrow t\bar{t}$  events. The background density  $O_B$  is based on Figure 5. For the innermost Forward Tracking Disk at the ILC one obtains the following average hit density:

$$O_p + O_B = 1 \times 10^{-4} \frac{\text{hits}}{\text{mm}^2} + 1.6 \times 10^{-4} \frac{\text{hits}}{\text{mm}^2 \text{BX}} (\text{average}). \quad (7)$$

This number reflects the number of charged particles traversing the corresponding detector element per unit area and time. It must be multiplied by the (average) number of channels that fires for each hit. As this is a technology-dependent quantity we do not include this factor here. Note that a threshold is applied for the energy deposition in the detectors that is also (mildly) technology dependent [45].

The hit density is subject to large event-to-event fluctuations. In the innermost detector layers jets can provoke a local occupancy that is two order of magnitudes larger than the average occupancy. The average occupancy moreover depends strongly on the position in the detector. The variation is particularly pronounced in the forward tracking disks, where the innermost ring has to deal with 10 times more background than the outer regions of the same disk. The peak hit density from signal and background in the innermost Forward Tracking Disk at the ILC then becomes:

$$O_p + O_B = 1 \times 10^{-2} \frac{\text{hits}}{\text{mm}^2} + 1.6 \times 10^{-3} \frac{\text{hits}}{\text{mm}^2 \text{BX}} (\text{peak values}). \quad (8)$$

Locally, in the core of jets, the contribution of physics event can exceed the background density from a single bunch crossing by an order of magnitude.

The relative contribution of the background hits depends on the technology chosen to equip the detector. At the ILC bunches cross every 500 ns. With fast electronics a single bunch crossing can be integrated and the high local density of signal events forms the tightest requirement. Micro-strip detectors are fast enough that single bunch crossings at the ILC can be identified. For 10 cm long, 50  $\mu\text{m}$  wide strips a peak occupancy of 6% per BX is obtained, which is well over the maximum (more on this in the discussion of ghost hits). Therefore, detectors with finer granularity are required. Several candidate technologies [46,47] can produce devices with a cell area of  $25 \times 25 \mu\text{m}^2$  and a read-out time of 50  $\mu\text{s}$ . The peak occupancy due to signal in the core of jets is less than  $10^{-5}$ , allowing for robust pattern recognition. When the background hits from approximately 100 bunch crossings are added, the total occupancy becomes  $1 \times 10^{-4}$ . The total occupancy remains at a comfortable level, as the very small pixel area (reduced by nearly four orders of magnitude) compensates for the increased integration time (100 bunch crossings as opposed to a single bunch crossing). The LC detector concepts have therefore opted for pixel detectors in the innermost Forward Tracking Disks.

An alternative solution is offered by the fine pixel CCD detectors [48] that integrate the 1312 bunch crossings of the bunch train. The occupancy is kept at an acceptable level by reducing the pixel size to below  $10 \times 10 \mu\text{m}^2$ .

At CLIC the bunch crossings are spaced by only 0.5 ns. It is assumed that the tracking and vertex detector integrate hits over the train duration of 156 ns.

Time stamping with a precision of 10 ns is sufficient to reduce the expected background occupancy to an acceptable level [10]. Low-mass and low-power hybrid pixel detectors with a pitch of approximately  $25 \times 25 \mu\text{m}^2$  [49] and a read-out architecture based on TimePix [50] are expected to achieve this requirement. Time stamping at the level of a single bunch crossing may be possible with specially designed, ultra-fast detectors.

For very shallow tracks we cannot rely on the quiet layers at large radial distance from the interaction point or the large number of measurements in the TPC. The presence of closely spaced detectors, where track candidates can be extrapolated to the following layer with an error of less than  $10 \mu\text{m}$ , and low occupancy, so that few new ambiguities arise, is crucial to sort out the ambiguities that inevitably arise in track finding. To increase the robustness of the forward system at CLIC the innermost forward tracking system is therefore formed by six closely spaced and highly granular disks [21].

## 7.2 Ghost hits

Micro-strip detectors remain the most economical option in terms of channel count and power density for large detector areas. In both cases the specification of the  $r\phi$  resolution is tightly constrained from the requirements on the momentum and transverse impact parameter resolution.

For micro-strip detectors in the forward region this argument naturally leads to the choice of radially oriented strips. To provide a precise measurement of the  $r\phi$ -coordinate that measures the track curvature the strips must be aligned with  $z$  in the cylindrical layers and radially along  $r$  in the disks. The constraint on the second coordinate ( $z$  and  $r$ , respectively) detector is very poor, as we can only infer that the particle traversed a given strip (typical sensors produced from 8 inch wafers are up to 10 cm long, often several sensors are ganged to produce even longer strips).

A more precise determination of the second coordinate is obtained if two measurements are combined. If the second sensor is rotated by  $90^\circ$ , the second coordinate is measured with the same resolution as the primary  $r\phi$  measurement. This configuration has, however, rather poor performance in a dense environment. Whenever more than one particle traverses a sensor, several *ghost* combinations appear that cannot be distinguished (using local information) from the three real hits. An example is shown in Figure 10. The total number of valid hit combinations scales with  $N^2$ , where  $N$  is the number of particles.

A solution to the problem of the ghost hits, adopted for example by the LHC experiments, is to use a small stereo angle of 40–100 milliradians. The combination of the two stereo measurements yields a determination of the second

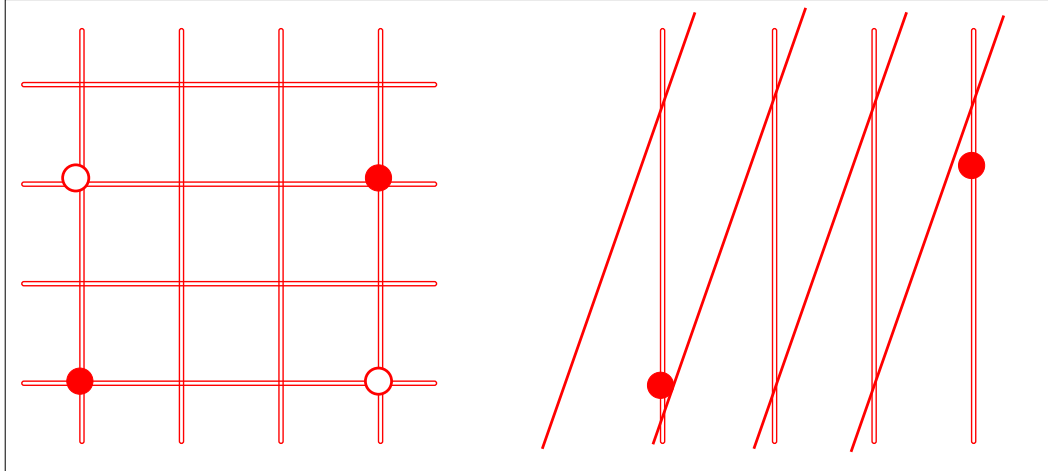


Fig. 10. Schematic representation of the formation of *ghost* hits in micro-strip detectors with 90 degree stereo angle (leftmost image). The incidence positions of two particles are indicated as filled red dots. Two additional valid combinations of the 1D information of both detectors are indicated as open circles. The rightmost image demonstrates how detectors at a 10 degree stereo angle produce no ghost hits in the same situation.

coordinate, with a precision that depends on the stereo angle (better resolution is achieved at larger angle). A more extensive discussion of the resolution is left for Section 7.3. The rightmost panel of Figure 10 shows that no ambiguities arise in the same situation as before if the strips are rotated by a 10 degree stereo angle. As each micro-strip overlaps with only a limited number of stereo strips, the probability to find a second hit in an overlapping stereo strip is greatly reduced.

Quantitatively, the ghost hit rate depends on the hit density in the detector and the detector design (pitch and sensor dimensions). In Figure 11 the number of ghost hits in in  $100 \times 100 \text{ mm}^2$  sensors with  $25 \mu\text{m}$  pitch is compared to the real occupancy due to particles incident on the sensor. The five curves correspond to stereo angles of from 1 milliradian to  $90^\circ$ . For a given stereo angle the ghost hit rate is negligible until a critical occupancy is reached. Beyond that point the rate increases very rapidly. Soon ghost hits are more abundant than the correct combinations and form an important source of confusion to the pattern recognition stage. The critical occupancy depends strongly on the stereo angle; smaller stereo angles help delay the onset of sufficient ghost hit contributions to large real occupancies. In practice, this feature of micro-strip detectors limits their use to environments where the occupancy is below the percent level. For the innermost disks in the LC detectors the peak occupancy is well above this level, adding yet another argument for the preference of pixelated devices in the innermost disks.

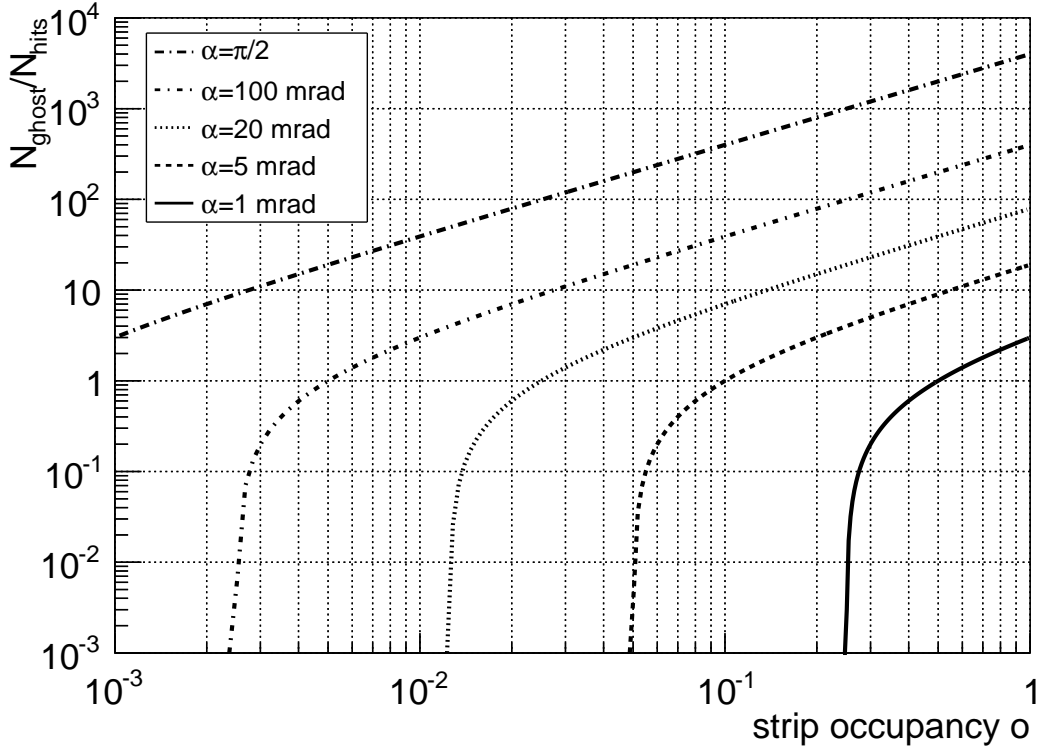


Fig. 11. The ratio of the number of ghost hits and the number of particles traversing the sensor versus strip occupancy. The curves correspond to five values of the stereo-angle, from 1 mrad to  $\pi/2$  rad.

### 7.3 Precision of the $r$ -measurement

The  $r\phi$  measurement is crucial for the determination of the particle momentum. The innermost layers, that play an important role in the reconstruction of the primary and secondary vertices, must measure a second coordinate to constrain the longitudinal impact parameter and polar angle of the trajectory. The measurement of the  $r$ -coordinate in the outermost disks, however, does not affect the final trajectory parameters significantly. The  $r$ -coordinate is measured to yield sufficient constraints on the trajectory for pattern recognition to converge.

In the previous section we have adopted a small stereo angle to avoid the presence of ghost hits. The combination of the two stereo measurements allows to reconstruct 2-dimensional space points, where the resolution on the  $r\phi$  and  $r$  coordinates is given<sup>3</sup> in terms of the space point resolution  $\sigma$  of each of the

<sup>3</sup> It is easy to see that these relations hold for the binary case, where  $\sigma = p/\sqrt{12}$ , but they hold quite generally. Consider two strips with pitch  $p$  that cross under an angle  $\alpha$ . The intersection forms a rhombus with short axis  $w = p/\cos(\alpha/2)$  and long axis  $h = p/\sin(\alpha/2)$ . The projection along these axes yields triangular distributions with  $RMS = w/\sqrt{24}$  and  $RMS = h/\sqrt{24}$ , hence the factor  $\sqrt{2}$  in the denominator.

measurements and the stereo angle  $\alpha$ :

$$\sigma(r\phi) = \frac{\sigma}{\sqrt{2} \cos(\alpha/2)},$$

$$\sigma(r) = \frac{\sigma}{\sqrt{2} \sin(\alpha/2)}$$

For small values of  $\alpha$  the  $r\phi$  measurement improves by a factor of approximately  $1/\sqrt{2}$ . The combination of both 1D measurements yields an  $r$  resolution of approximately  $\frac{\sigma}{2\alpha}$ . For  $\alpha = 100$  mrad, the  $r$  resolution is  $20 \sigma$ , i.e. approximately  $100 \mu\text{m}$  in typical detectors.

During the track finding phase a seed is grown into a full-length track by extrapolation to the following layer and addition of compatible hits. A poor measurement of the  $r$ -coordinate render the extrapolation to the following layer inaccurate. If the uncertainty on the extrapolated position increases too much, many spurious hits may be found compatible with the poorly constrained trajectory of the track stub.

To quantify this argument we propagate seeds generated in either highly granular or low-density regions<sup>4</sup> with a rudimentary implementation of the combinatorial algorithm used in the LHC experiments. Each seed is propagated to the next layer with the Kalman filter also used for the final track fit. If a hit is found whose location is compatible with the extrapolated position within error, the hit is added to the track stub and propagated to the next layer. If no compatible hits are encountered, the candidate is not propagated further<sup>5</sup>. If multiple hits are found, a new track candidate is spawned for each compatible hit, and all track candidates are propagated in parallel (hence the name combinatorial). If sufficient constraints are available, the *fake* candidates encounter no compatible hits on further layers and do not grow into full-length tracks. However, if the probability to add spurious hits is non-negligible in all layers, or the number of layers is limited, the resulting confusion may not be resolved.

As an example, we consider inside-out track finding in three pixel disks and four micro-strip disks. The distance between disk 1 and 2, 2 and 3, and 3 and 4 is 11 cm. From there on, the distance is increased to 25 cm. All layers measure  $r\phi$  with  $10 \mu\text{m}$  precision. The pixel disks achieve the same precision in  $r$ , while the micro-strip disk provide no constraints on  $r$ . The uncertainty

<sup>4</sup> The former option corresponds to *inside-out* track reconstruction, starting from the vertex detector and pixel disks, while *outside-in* reconstruction starts from the outer silicon micro-strip layers located in the region with lower hit density

<sup>5</sup> In real-life implementations a limited number of missing hits is allowed to account for inefficiency of the detector layers. Here, no inefficiencies are simulated and a hit must be found on each layer that is crossed.



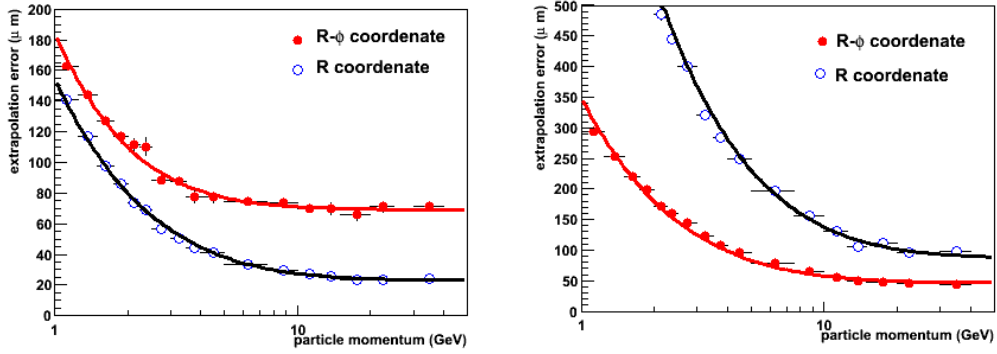


Fig. 12. The uncertainty on the extrapolated  $r\phi$ - (closed markers) and  $r$ -coordinate (open markers). The leftmost panel corresponds to the extrapolation of a pixel triplet to the fourth disk. The rightmost panel corresponds to the extrapolation from the 5th to the 6th disk.

in the  $r\phi$ - and  $r$ -coordinate is shown in Figure 12 as a function of particle momentum for two different steps in the inside-out pattern recognition process. The leftmost panel corresponds to the extrapolation over 11 cm of a triplet of pixel detector hits to the fourth tracking disk. Three precise measurements of the  $r$ -coordinate are sufficient to constrain the trajectory in the  $rz$  projection (where the track model reduces to a straight line in the high momentum limit). The three equally precise  $r\phi$  measurements provide a poor constraint of the track curvature, due to the short lever arm of the first disks. Therefore, the  $r\phi$  measurement is predicted with relatively poor precision. The rightmost panel shows the situation after the track candidates are propagated through another couple of disks equipped with micro-strip detectors. To clearly show the difference, these detectors are assumed to measure only the  $r\phi$ -coordinate. As a consequence of the addition of two further points with precise  $r\phi$  measurements and large lever arm the  $r\phi$ -prediction is improved considerably for high momentum tracks. At low momentum the large separation of the disks degrades the precision considerably. The  $r$ -measurement, on the other hand, is degraded very strongly. The lack of further measurements to constrain the relevant degrees of freedom of the track fit leads to a steady growth of the uncertainty of the extrapolation.

The precision with which track seed and stubs can be extrapolated to the next layer is crucial for pattern recognition. If the uncertainty in the extrapolated position can be kept to a minimum, few spurious hits are compatible (within errors) with the trajectory. A quantitative marker is the area of the error ellipse in each extrapolation step. The axes of the ellipse are given by the uncertainties in  $r$  and  $r\phi$  position of the extrapolated track. Any hit in the area of the ellipse must be assigned to the track.

In Reference [21] the area of the error ellipse in outside-in track finding is evaluated for different assumptions on the precision of the  $r$ -measurements of the

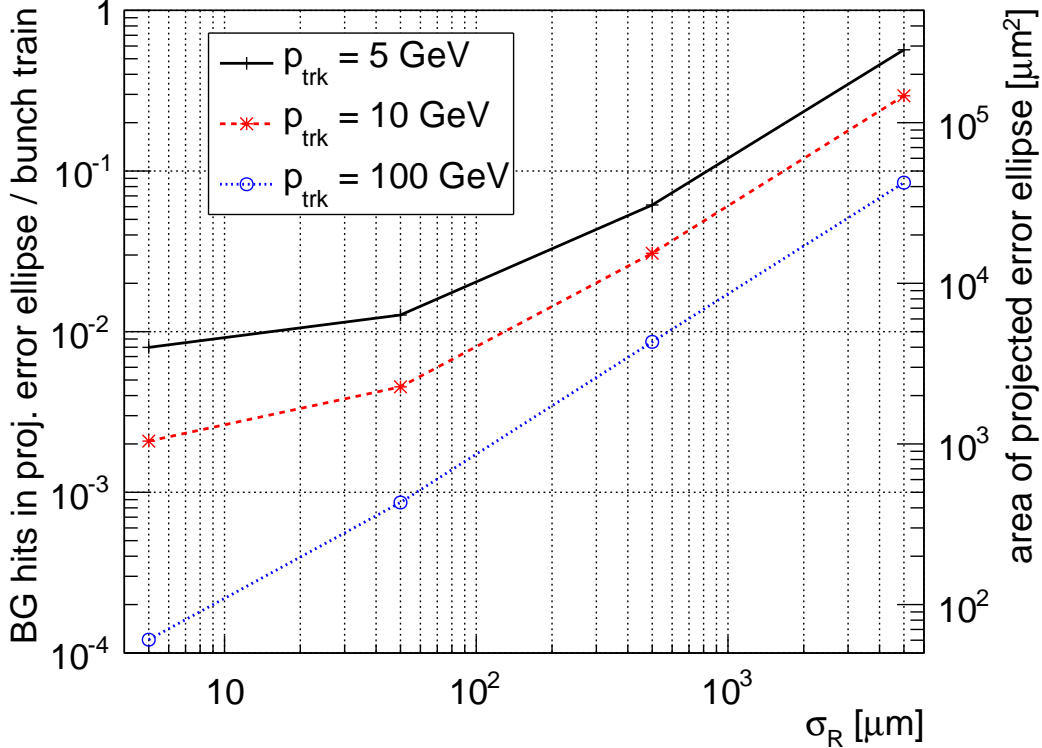


Fig. 13. Expected background hit rates inside track-extrapolation error ellipses projected from a track stub formed by measurements on six  $\mu$ -strip disks onto the outermost forward pixel layers. The  $r\phi$ -resolution is fixed at  $5\ \mu\text{m}$  and the resolution in  $r$  is varied between  $5\ \mu\text{m}$  and  $5\ \text{mm}$ . The scale on the right axis gives the area of the respective error ellipses. The background occupancy is assumed to be 2 hits per  $\text{mm}^2$  and bunch train.

forward tracking system. In Figure 13, the area of the error ellipse on disk  $N$  is shown. The x-axis ranges from an  $r$ -resolution below  $10\ \mu\text{m}$ , corresponding to highly granular devices with rectangular pixels, to the poor  $r$ -measurement of micro-strip detectors with a small stereo angle. The intermediate region corresponds to elongated pixels with an  $r$ -dimension of several  $100\ \mu\text{m}$ . A second scale indicates how many background hits are typically found within this area, which is a good measure of the confusion term in each pattern recognition step. The result for high momentum tracks is indicated by the (blue) dotted curve. In this case the area depends linearly on the  $r$ -resolution. For low-momentum tracks the confusion increases. A clear saturation is moreover observed, as at one point the multiple scattering contribution to the uncertainty prevents further improvement of the extrapolated position. This result shows that a precise  $r$ -measurement can render pattern recognition much more robust. Beyond an  $r$ -precision of the order of  $100\ \mu\text{m}$  little is gained for low momentum tracks, that are the hardest to reconstruct efficiently and cleanly. We conclude, therefore, that the design of the forward region should aim for moderately precise  $r$ -measurements in all tracking layers.

A number of stress tests have been performed to evaluate how strongly the standalone pattern recognition performance of the Forward Tracking Disks depends on the design assumptions. A strong increase in the material or in the read-out time can degrade the pattern recognition performance to an unacceptable level.

In the forward tracking system, pattern recognition must converge after only a small number of measurements separated by large distances. The devices that equip the Forward Tracking Disks should provide two-dimensional space points to reduce the ambiguities in the track finding stage. We find that the  $r$  measurement with moderate precision that is readily provided by micro-strip detectors with a small stereo angle is adequate for this purpose.

## 8 Summary & conclusions

In a previous paper [19] we have argued that as  $e^+e^-$  colliders are built to reach higher and higher center-of-mass energy, the relevance of the forward and backward regions of the detector design for the overall performance of the experiment increases considerably.

In this work we identify the main challenges of the forward tracking system and relate them to the detector design in a quantitative fashion.

The transverse momentum resolution is degraded in the forward region, approximately as  $1/\sin^{3/2}\theta$ , due to the unfavourable orientation of the magnetic field. To maintain good performance for tracks emitted at small polar angle, emphasis should be given to the development of detectors with excellent spatial resolution for the  $r\phi$ -coordinate, while maintaining the strict material budget.

The vertex reconstruction performance for charged particles emitted at small polar angle is also degraded. An endcap detector equipped with precise and thin pixel detectors can check the  $1/\sin\theta^{3/2}$  growth of the impact parameter resolution, but this requires a very strict control of the material in the beam pipe and the services and support in the barrel-endcap transition.

Efficient and clean track reconstruction demands highly granular devices in the innermost regions of the detector, where the background density is highest. Robust pattern recognition moreover requires the determination with moderate precision of the  $r$ -coordinate of hits in all forward tracking layers.

## 9 Acknowledgements

This work has been partly supported by Grants FPA2010-22163-C02-01 and FPA2010-21549-C04-4 of the Spanish Ministry of Economy and Competitiveness; and by the European Commission within Framework Programme 7 Capacities, Grant Agreement 262025 (AIDA). We would like to acknowledge the ILD software group that developed many of the tools used to obtain the reported results. M. Vos would moreover like to thank the LCD group at CERN for their hospitality.

## References

- [1] **The ILC community**, E. Brau, James et al., *ILC Reference Design Report: ILC Global Design Effort and World Wide Study*, [arXiv:0712.1950](#).
- [2] M. Aicheler et al., *A Multi-TeV Linear Collider based on CLIC Technology: CLIC Conceptual Design Report*, [EDMS link](#).
- [3] J. E. Brau, R. M. Godbole, F. R. L. Diberder, M. Thomson, H. Weerts, et al., *The Physics Case for an  $e^+e^-$  Linear Collider*, [arXiv:1210.0202](#).
- [4] **The ILC community**, G. Aarons et al., *ILC Reference Design Report Volume 2: physics at the ILC*, [arXiv:0709.1893](#).
- [5] **American Linear Collider Working Group**, T. Abe et al., *Linear collider physics resource book for Snowmass 2001. 1: Introduction*, [hep-ex/0106055](#).
- [6] **American Linear Collider Working Group**, T. Abe et al., *Linear collider physics resource book for Snowmass 2001. 2: Higgs and supersymmetry studies*, [hep-ex/0106056](#).
- [7] **American Linear Collider Working Group**, T. Abe et al., *Linear collider physics resource book for Snowmass 2001. 3: Studies of exotic and standard model physics*, [hep-ex/0106057](#).
- [8] **American Linear Collider Working Group**, T. Abe et al., *Linear collider physics resource book for Snowmass 2001. 4: Theoretical, accelerator, and experimental options*, [hep-ex/0106058](#).
- [9] **ECFA/DESY LC Physics Working Group**, J. A. Aguilar-Saavedra et al., *TESLA Technical Design Report Part III: Physics at an  $e^+e^-$  Linear Collider*, [hep-ph/0106315](#).
- [10] L. Linssen, A. Miyamoto, M. Stanitzki, and H. Weerts, *Physics and Detectors at CLIC: CLIC Conceptual Design Report*, [arXiv:1202.5940](#).
- [11] P. Lebrun, L. Linssen, A. Lucaci-Timoce, D. Schulte, F. Simon, et al., *The CLIC Programme: Towards a Staged  $e^+e^-$  Linear Collider Exploring the Terascale : CLIC Conceptual Design Report*, [arXiv:1209.2543](#).

- [12] **CLIC Physics Working Group**, E. Accomando et al., *Physics at the CLIC multi-TeV linear collider*, [hep-ph/0412251](#).
- [13] **ATLAS Collaboration**, *Observation of a new particle in the search for the Standard Model Higgs boson with the ATLAS detector at the LHC*, *Phys.Lett. B* **716** (2012) 1–29, [[arXiv:1207.7214](#)].
- [14] **CMS Collaboration**, *Observation of a new boson at a mass of 125 GeV with the CMS experiment at the LHC*, *Phys.Lett. B* **716** (2012) 30–61, [[arXiv:1207.7235](#)].
- [15] **LHC/LC Study Group**, G. Weiglein et al., *Physics interplay of the LHC and the ILC*, *Phys. Rept.* **426** (2006) 47–358, [[hep-ph/0410364](#)].
- [16] **The ILC community**, E. . Behnke, Ties et al., *ILC Reference Design Report Volume 4 - Detectors*, [arXiv:0712.2356](#).
- [17] **ILD Concept Group**, T. Abe et al., *The International Large Detector: Letter of Intent*, [arXiv:1006.3396](#).
- [18] E. Aihara, H., E. Burrows, P., E. Oreglia, M., E. Berger, V. Guarino, et al., *SiD Letter of Intent*, [arXiv:0911.0006](#).
- [19] J. Fuster, S. Heinemeyer, C. Lacasta, C. Marinas, A. Ruiz Jimeno, et al., *Forward tracking at the next  $e^+ e^-$  collider. Part I. The Physics case*, *JINST* **4** (2009) P08002, [[arXiv:0905.2038](#)].
- [20] **ILD concept group**, *The International Large Detector: Detailed Baseline Design*. 2013. to appear.
- [21] D. Dannheim and M. Vos, *Simulation studies for the layout of the vertex and tracking regions of the CLIC detectors*, . LCD-NOTE-2011-031.
- [22] M. Regler, W. Mitaroff, M. Valentan, R. Fruhwirth, and R. Hoffer, *The 'LiC Detector Toy' program*, *J. Phys. Conf. Ser.* **119** (2008) 032034.
- [23] **GEANT4 Collaboration**, S. Agostinelli et al., *GEANT4: A simulation toolkit*, *Nucl. Instrum. Meth.* **A506** (2003) 250–303.
- [24] P. Mora de Freitas and H. Videau, *Detector simulation with MOKKA / GEANT4: Present and future*, . LC-TOOL-2003-010.
- [25] F. Gaede, *Marlin and LCCD: Software tools for the ILC*, *Nucl.Instrum.Meth.* **A559** (2006) 177–180.
- [26] S. Aplin, J. Engels, F. Gaede, N. A. Graf, T. Johnson, et al., *LCIO: A Persistency Framework and Event Data Model for HEP*, .
- [27] S. Aplin, F. Gaede, and R. Glattauer, *The New C++ Tracking Code in iLCSoft*, . LCWS12, Arlington, Texas, USA.
- [28] R. Glattauer, R. Fruhwirth, J. Lettenbichler, and W. Mitaroff, *Forward Tracking in the ILD Detector*, [arXiv:1202.2761](#).

- [29] “<http://www.slac.stanford.edu/~schumm/lcdtrk20011204.tar.gz>.”
- [30] P. Billoir, *Track fitting with multiple scattering: a new method*, *Nucl.Instrum.Meth.* **A225** (1984) 352–366.
- [31] D. Schulte et al., *GUINEA PIG++ : An Upgraded Version of the Linear Collider Beam Beam Interaction Simulation Code GUINEA PIG*, . Particle Accelerator Conference PAC07 25-29 Jun 2007, Albuquerque, New Mexico.
- [32] C. Rimbault, P. Bambade, K. Monig, and D. Schulte, *Study of incoherent pair generation in guinea-pig*, . EUROTEV-REPORT-2005-016.
- [33] D. Schulte, *Beam-beam simulations with guinea-pig*, . CERN-PS-99-014-LP; CLIC-Note-387.
- [34] D. Dannheim and A. Sailer, *Beam-Induced Backgrounds in the CLIC Detectors*, . LCD-NOTE-2011-021.
- [35] H. Li, F. Richard, R. Poeschl, and Z. Zhang, *Precision Measurements of SM Higgs Recoil Mass and Cross Section for  $s^{*1/2}$  of 230-GeV and 250-GeV at ILC*, [arXiv:0901.4893](https://arxiv.org/abs/0901.4893).
- [36] C. Greife, T. Lastovicka, J. Strube, F. Teubert, and B. Pie Valls, *Measurement of the Cross Section Times Branching Ratio of Light Higgs Decays at CLIC*, [arXiv:1202.5647](https://arxiv.org/abs/1202.5647).
- [37] C. Greife, T. Lastovicka, and J. Strube, *Prospects for the Measurement of the Higgs Yukawa Couplings to b and c quarks, and muons at CLIC*, [arXiv:1208.2890](https://arxiv.org/abs/1208.2890).
- [38] **ALEPH** Collaboration, D. Buskulic et al., *Performance of the ALEPH detector at LEP*, *Nucl. Instrum. Meth.* **A360** (1995) 481–506.
- [39] **DELPHI** Collaboration, P. Abreu et al., *Performance of the DELPHI detector*, *Nucl. Instrum. Meth.* **A378** (1996) 57–100.
- [40] **CMS** Collaboration, G. L. Bayatian et al., *CMS physics: Technical design report*, . CERN-LHCC-2006-001.
- [41] **ATLAS** Collaboration, . G. Aad et al., *Expected Performance of the ATLAS Experiment - Detector, Trigger and Physics*, [arXiv:0901.0512](https://arxiv.org/abs/0901.0512).
- [42] M. Valentan, M. Regler, W. Mitaroff, and R. Fruhwirth, *LiC Detector Toy - Tracking detector optimization with fast simulation and its application to the ILD design*, [arXiv:0901.4183](https://arxiv.org/abs/0901.4183).
- [43] R. Gluckstern, *Uncertainties in track momentum and direction, due to multiple scattering and measurement errors*, *Nucl.Instrum.Meth.* **24** (1963) 381–389.
- [44] V. L. Highland, *Some Practical Remarks on Multiple Scattering*, *Nucl.Instrum.Meth.* **129** (1975) 497.

- [45] D. Dannheim, A. Sailer, J. Trenado, and M. Vos, *CLIC Background Studies and optimization of the innermost tracker elements*, [arXiv:1203.0942](#).
- [46] **DEPFET** Collaboration, O. Alonso et al., *DEPFET active pixel detectors for a future linear  $e^+e^-$  collider*, [arXiv:1212.2160](#).
- [47] M. Winter, J. Baudot, A. Besson, G. Claus, A. Dorokhov, et al., *Development of CMOS Pixel Sensors fully adapted to the ILD Vertex Detector Requirements*, [arXiv:1203.3750](#).
- [48] Y. Sugimoto, H. Ikeda, D. Kamai, E. Kato, A. Miyamoto, et al., *R & D Status of FPCCD Vertex Detector for ILD*, [arXiv:1202.5832](#).
- [49] P. Valerio, *CLICpix demonstrator design*, [EDMS link](#).
- [50] K. Akiba, M. Artuso, R. Badman, A. Borgia, R. Bates, et al., *Charged Particle Tracking with the Timepix ASIC*, *Nucl.Instrum.Meth.* **A661** (2012) 31–49, [[arXiv:1103.2739](#)].